Biosensors and Bioelectronics 132 (2019) 186–195

Contents lists available at ScienceDirect

Biosensors and Bioelectronics

journal homepage: www.elsevier.com/locate/bios

A signal-on nanobiosensor for $VEGF_{165}$ detection based on supraparticle copper nanoclusters formed on bivalent aptamer

Fatemeh Mortazavi Moghadam, Mahdi Rahaie*

Department of Life Science Engineering, Faculty of New Sciences and Technologies, University of Tehran, Postal Code 1439957131, Iran

ARTICLE INFO

Keywords:
Nanobiosensor
Bivalent aptamer
Cu nanocluster
$VEGF_{165}$
Target-induced structure switching mode
Aggregation-induced emission

ABSTRACT

In this study, a signal-on nanobiosensor based on bivalent aptamer-Cu nanocluster was designed and optimized for specific and sensitive detection of $VEGF_{165}$. The $VEGF_{165}$ is known as a promising biomarker in different diseases such as cancer in the angiogenic stage. Detection and quantification of $VEGF_{165}$ is a crucial step in diagnosis and monitoring the treatment plan. The represented nanostructure consists of multimerized $VEGF_{165}$ aptamer joint with ssDNA based linker in the middle and poly thymine sequences on both 3′ and 5′ ends as a template for Cu-nanocluster supraparticle formation. This self-assembled structure leads to accurate controlling of aggregation in the presence of $VEGF_{165}$. This study is the first report for Cu nanocluster nucleation on ploy thymine tails of ssDNA which performed in two reduction steps to form stable CuNC supraparticle. The sensing strategy was designed based on the target-induced structure switching mode of the aptamer. In the presence of $VEGF_{165}$, due to self-assembly induced emission and aggregation-induced emission phenomena this nanostructure depicted the visible wavelength shift and enhancement in the fluorescence emission intensity. Also, the results of the analytical performance of this nanobiosensor indicated the LOD of 12 pM which revealed high rate sensitivity. This aptasensor exhibited stability and decent response linearity range (10–800 pM, R^2 = 0.9943). The selectivity and specificity assessment showed high discriminant capability in the real serum sample. In conclusion, this signal-on nanobiosensor provides a facile, sensitive and reliable assay for clinical monitoring of the $VEGF_{165}$ concentration in serum without further sample preparation.

1. Introduction

Based on the nanometric scale in noble metal nanoclusters which comprise tens of atoms, the molecule-like behavior of Cu Nanoclusters propinquity with electrons Fermi wavelength and intraband HOMO-LUMO transition inward the SP band creates unique photo-physical characteristics in this type of nanostructures (Liu et al., 2018). Wide variety range of Cu nanoclusters applications in biosensing, biolabeling, and fluorescence analysis is beholden to individual photic behavior exceptionally strong fluorescent properties (Dutta et al., 2018). The Presence of Cu nanoclusters in the close distance as supraparticles structure increase the capability of this assembly as an efficient transducer. The ordered dispersed nanostructure assembly with a specific array defined as supraparticles (Wintzheimer et al., 2018).

Recently, specific biomolecules such as proteins, especially Bovine serum albumin (BSA) (Bagheri et al., 2017) and short sequence of DNA have been applied as templates to synthesize noble metallic nanoclusters (Mahmoudi et al., 2019). The function of a protein directly depends on its three-dimensional conformation. In basic pH which is necessary for copper nanocluster formation, the isoelectric condition of protein change, which leads to inefficiency in the function of protein and causes some limitations in functional biosensing application of the structures.

The configuration of the specific supraparticle structure on the termini of the ssDNA could play dual roles as a biorecognition component and transducer moiety, simultaneously.

The changes in conformation due to the interaction of biorecognition part with analyte, transform to the measurable signal by transducer. Minimizing the distance between transducer and biorecognition part leading to improvement in biosensing performance. For this specific biorecognition function, ssDNA based aptamer because of stability in temperature and different pH values, higher specificity, versatility in the modification, capability for assembling multimeric structure, controllable aggregation and the ability of specific sequence as reduction agent, is considered as an appropriate option (Kong et al., 2015). Some of the particular aptamers indicated an extraordinary affinity for specific protein biomarkers (Stoll et al., 2017). One of this critical biomarker in advanced disease is vascular endothelial growth factor

* Corresponding author.
E-mail address: mrahaie@ut.ac.ir (M. Rahaie).

https://doi.org/10.1016/j.bios.2019.02.046
Received 23 December 2018; Received in revised form 6 February 2019; Accepted 14 February 2019
Available online 26 February 2019
0956-5663/

(VEGF) (Yang et al., 2018). Studies revealed numerous Angiogenesis regulators consisting of; TGFα, TGFβ, TNFα, HGF/SF, aFGF, bFGF, VEGF, Angiogenin, Where VEGF plays the dominant role in pathological and normal Angiogenesis (Dehghani et al., 2018). The VEGF gene in *Homo sapiens* on 6p21.3 chromosome includes eight exons and seven introns; alternative exon splicing leads to generate four different species, $VEGF_{121}$, $VEGF_{165}$, $VEGF_{189}$, $VEGF_{206}$ and the absence of residue encoded by exon 6 creates $VEGF_{165}$ (Wang et al., 2009). The $VEGF_{165}$ is known as VEGF-A and plays the crucial role as an indicator in age-related macular degeneration (AMD) (Ju et al., 2008), diabetic retinopathy (DR) (Makarevich et al., 2015), Rheumatoid arthritis (Alam et al., 2014), proteinuria (Bus et al., 2017) and angiogenic stage of cancer tumor (Chen et al., 2016). Distinguish of the $VEGF_{165}$/A from other species and accurate quantification of it overexpression as a function depends on its concentration in advanced diseases is the indispensable requirement, and the Target-induced structure switching mode (TISS) (Han et al., 2010) aptamer based nanobiosensor could be considered to be a feasible option. In TISS aptasensor, $VEGF_{165}$ directly binds to the aptamer and changing the conformational structure induces the detectable signal. For obtaining this goal in this study, the multimer structure of aptamer designed. The represented multimer ssDNA aptamer consists of two specific sequences with the affinity to $VEGF_{165}$, linker in the middle and two poly T sequences in both 3′ and 5′ ends considered as Cu nanocluster nucleation zone. During two steps copper reduction which revealed for the first time in this study, Cu ions bound exclusively on the thymine and formed Cu nanocluster supraparticle array on the both 3′ and 5′ ends of aptamer. In the presence of $VEGF_{165}$, Cu nanocluster supraparticle positioned in close distance and Self-assembly induced emission (SAIE) and Aggregation-induced emission (AIE) phenomena as fluorescence enhancement mechanisms create signal-on nanobiosensor (Scheme 1).

Based on our best of knowledge, this study is the first report for signal-on based nanobiosensor for $VEGF_{165}$ detection via supraparticle Cu nanocluster formed on both 3′ and 5′ tails of ssDNA aptamer for detecting $VEGF_{165}$ in real serum sample. This structure plays a role as biorecognition part and transducer moiety, simultaneously.

2. Experimental

2.1. Reagents

All chemicals were in analytical grade and used without further purification. All aqueous solutions was prepared by deionized water For the effect of ions elimination (MilliporeSigma AFS®D Water Purification System). HEPES buffer was purchased from Gibco life science (USA). Cupric sulfate pentahydrate ($CuSo_45H_2O$), L-Ascorbic acid, Tris, Boric acid and EDTA were provided from Merck (Germany).

The ssDNA strands which used in this study were synthesized, purified by HPLC and quality control via MALDI-TOF in Bioneers (Daejeon, Korea). The sequence of aptamer was mentioned in the S1 Table. Recombinant human $VEGF_{165}$ with 38.2 kDa molecular weight as a disulfide-linked homodimeric protein includes two 165 amino acid polypeptide chains, was purchased from Abcam (USA). The full-length sequence of mature protein minus the signal peptide was mentioned in the S2 Table. Natural Human Serum Albumin protein (HSA), Bovine Serum Albumin Protein (BSA), The IGF-1, Recombinant Human (HB), EGF protein, IgG, IgE provided from Abcam (USA).

2.2. The Cu-NCs supraparticles on ssDNA aptamer synthesis

The $CuSo_45H_2O$ (0.1 M) solved in HEPES buffer (1 M, 1 mL, pH = 7.0) and added dropwise in L-Ascorbic acid (1 M, 10 mL) under vigorous stirring. The mixture kept in 70 °C for 1 h in a closed system. Subsequently, in the second step 500 µl of the reduced ion was added to ssDNA (100 µl, 1025.3 ng/µl, 260/280 ratio was 1.65). The solution kept in room temperature for 7 h. Before running the assays, the Bivalent Aptamer copper nanocluster (B-Apt-CuNC) was heated in the Benmary (80.4 °C) for 2 min and let it cool at room temperature. The Bivalent Aptamer copper nanocluster 500 µl mixed with $VEGF_{165}$ (200 pM, 300 µl) for preparing Bivalent Aptamer copper nanocluster with $VEGF_{165}$ (B-Apt-CuNC-$VEGF_{165}$).

2.3. Apparatus and sample preparation

Each spectrum has represented the mean of three different replicate experiments with each performed in triplicate.

2.3.1. DLS

the samples for DLS measurement prepared by dilution in HEPES buffer (pH = 7.0). 200 µl of B-Apt-CuNC diluted in 2800 µl HEPES buffer and The 200 µl of Bivalent Aptamer copper nanocluster with $VEGF_{165}$ as a complex diluted in 2800 µl HEPES buffer. The size of the samples was measured by Dynamic Light Scattering SZ100 Horiba (Horiba, Japan).

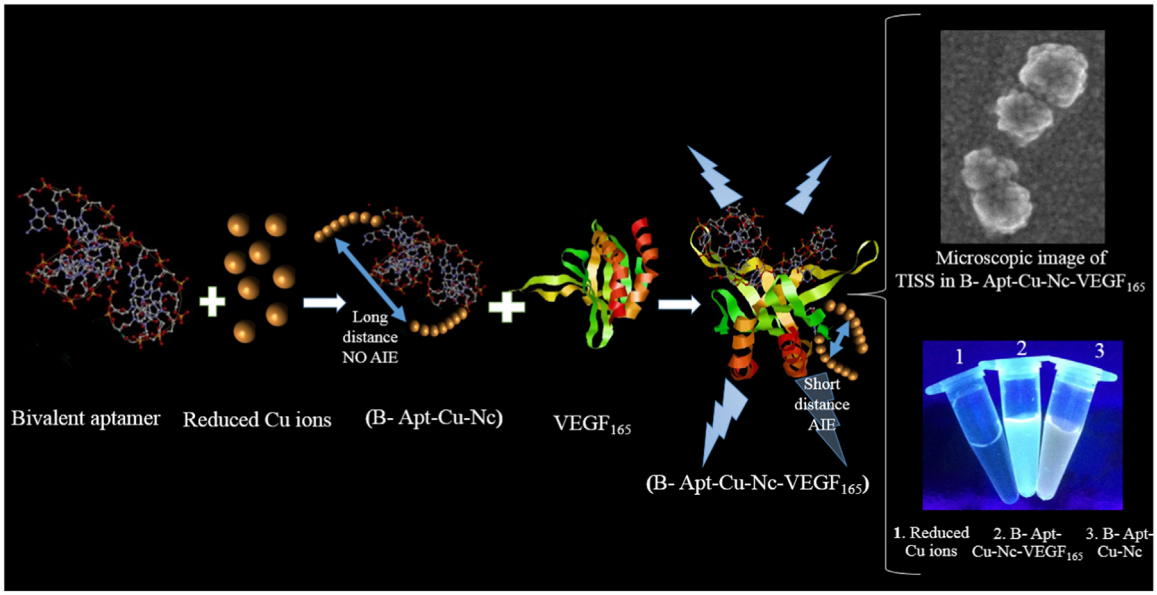

Scheme 1. Formation of copper nanocluster on bivalent aptamer and AIE in the presence of $VEGF_{165}$.

2.3.2. Uv visible spectroscopy

The UV visible absorption measurement was performed by Microvolume Spectrophotometers NanoDrop ND-2000C (Thermo scientific, USA). The absorption of B-Apt-CuNC 200 µl in 2800 µl HEPES buffer and B-Apt-CuNC-VEGF$_{165}$ 200 µl in 2800 µl HEPES buffer were measured in the 200–800 nm wavelength range.

2.3.3. Microscopic study

The HRTEM Tecnai G2 F30 with an acceleration voltage of 300 kV and 0.18 nm spatial resolution (FEI, USA) was used for microscopic studies. A drop of sample put on copper grid coated by carbon film surface and dried overnight at room temperature. The product of the first step reduction of copper salt (R-Cu) and B-Apt-CuNC-VEGF$_{165}$ selected as samples for microscopic study.

2.3.4. Photography

Photography of samples under UV radiation was performed in gel documentation chamber E-BOX-VX2/20MX via camera Sony DSC-H300 20.1 megapixel 35x optical zoom. The R-Cu (500 µl), B-Apt-CuNC (500 µl), B-Apt-CuNC-VEGF$_{165}$ (500 µl) chosen as samples for photography.

2.3.5. Circular Dichroism

CD spectra were acquired in 224–320 nm with 1.2 nm intervals by Circular Dichroism Aviv 215 (Aviv, USA) in the room temperature with 100 nm/min^{-1} scanning speed. 50 µl of bare bivalent aptamer as control, VEGF$_{165}$ protein as control, B-Apt-CuNC and B-Apt-CuNC-VEGF$_{165}$ samples diluted in HEPES buffer 250 µl measured by microvolume (300 µl) quartz cuvette. For homogenizing the samples before measurement, pipetting was performed for all samples.

2.3.6. MALDI-TOF

The B-Apt-CuNC-VEGF$_{165}$ aggregation was studied by ABCIES 4800 MALDI–TOF. The Matrix-assisted laser desorption ionization-time of flight (MALDI-TOF) in soft condition (Gast et al., 2011) was used to analyze the B-Apt-CuNC-VEGF$_{165}$ aggregation to clarify the effect of the presence of VEGF$_{165}$. Sample preparation in brief; B-Apt-CuNC-VEGF$_{165}$ was purified by reversed phase chromatography. Purified sample (6 µl) was spotted on MALDI-target, coated by 6 µl of 1% sinapinic acid in acetone. In the next step, 6 µl of 1% sinapinic acid in 40% acetonitrile was added.

2.3.7. Electrophoresis

To confirm the Cu-NC formation on ssDNA aptamer 5 µl of samples loaded in 4 wells on 3% agarose gel for electrophoresis. The staining was not performed due to the fluorescent activity of copper nanocluster (Zhu et al., 2015). The samples mixed with 15% glycerol (3 µl) to induce heaviness in samples and loaded in lanes without further procedure. The bare aptamer as the control without any copper nanocluster stained with Gel Red 6×. Electrophoresis was run by SUB 17 * 20 &amp (Paya Pajoohesh, Iran) at 70 V for 50 min in 1× TBE buffer (0.89 m Tris, 0.89 m Boric acid and 0.02 m EDTA pH 8.4). Gel photography performed by gel documentation chamber (QUANTUM ST4, Fisher Biotech Pty Ltd, Australia).

2.4. Spectrofluorimetric studies

The fluorescence emission spectra were recorded by LS45 Fluorescence Spectrometer PerkinElmer (Perkin Elmer, USA) by 1 cm path length quartz microcuvette from 300 to 650 nm wavelength. The excitation wavelength for B-Apt-CuNC and B-Apt-CuNC-VEGF$_{165}$ was set at 333 nm and 400 nm, respectively.

2.4.1. The calibration curve

The calibration experiment was run by constant volume of B-Apt-CuNC 200 µl and titrated with increasing concentrations of VEGF$_{165}$ (10–800 pM, 100 µl) at room temperature. Emission spectra were recorded with a scanning speed of 100 nm min^{-1}. The fluorescence results were calculated by (I/I_0) from the plot of (I/I_0) at 520 nm against concentration by using the Stern-Volmer equation.

$$\boldsymbol{I/I_0 = 1 + Ksv\,[Q]}$$

Where I is the fluorescence intensity in the presence of VEGF$_{165}$ and I_0 is the fluorescence intensity in the absence of VEGF$_{165}$ and the concentration of VEGF$_{165}$ demonstrated by [Q].

2.4.2. Fluorescence study of B-Apt-CuNC

The Fluorescence spectra of different B-Apt-CuNC with different ssDNA concentrations (500 ng/ul, 1025.3 ng/ul, 1550.1 ng/ul) in HEPES buffer (300 µl) were taken. The concentration of each ssDNA sample measured in 260 nm wavelength by the UV visible Microvolume Spectrophotometer (NanoDrop ND-2000C, Thermo scientific, USA). Then the B-Apt-CuNC synthesized in the same condition and different ssDNA concentration (500 ng/ul, 1025.3 ng/ul, 1550.1 ng/ul). The excitation wavelength for B-Apt-CuNC was set at 333 nm.

2.4.3. Fluorescence study of B-Apt-CuNC selectivity assay

The selectivity of B-Apt-CuNC (200 µl) was assessed by fluorescence emission intensity in the presence of Human Serum Albumin protein (HSA) (200 pM), Bovine Serum Albumin Protein (BSA) (200 pM), The IGF-1 (200 pM), Recombinant Human HB (200 pM), EGF protein (200 pM), IgG (200 pM), IgE (200 pM) and VEGF$_{165}$ (200 pM) in HEPES buffer(300 µl, pH7) separately. The Selectivity assessment for represented nanobiosensor was performed in room temperature for 40 min. The binding specificity of the B-Apt-CuNC for VEGF$_{165}$ in comparison to other abundant proteins in serum is elucidated by assessing the fluorescence signal. The selectivity and interaction of B-Apt-CuNC to target and nontarget proteins was assigned as a 100% relative fluorescence response.

2.4.4. Optimization the incubation time by fluorescence emission

Experiments were conducted to optimize the incubation time of the B-Apt-CuNC-VEGF$_{165}$ complex for 60 min at room temperature. The B-Apt-CuNC 500 µl mixed with VEGF$_{165}$ (200 p.M.,300 µl) for preparing B-Apt-CuNC-VEGF$_{165}$. the fluorescence emission intensity measured during incubation Period (5–10 min - 20–30 min - 40–50–60 min).

2.4.5. Quantum yield calculation

The fluorescence quantum yields of B-Apt-CuNC was calculated according to the formula;

$$\boldsymbol{\varphi X = \varphi s\left(\frac{Fx}{Fs}\right)\left(\frac{As}{Ax}\right)\left(\frac{\eta x2}{\eta s2}\right)}$$

The F_X and F_S refer to integrated area under emission profile for sample and standard. The absorbance quantity demonstrated by A_X and A_S for sample and standard solution. η indicates the refractive index of the solvent.

3. Results and discussion

Fluorescence based biosensor has many advantages over the alternative biosensor including simplicity, high sensitivity (Qu et al., 2017) and none sample destructive (Zhang et al., 2017). Turn-On mechanism in biosensing is considered as the promising strategy (Li et al., 2017). The advantages of light-on strategy precedence over light-off in the sensing viewpoint are included low background variation, the minimum rate of the false signal and abundant room for signal changes (Chen et al., 2014; Pei et al., 2015). In current fluorescence nanobiosensor, fluorescent proteins, organic dyes and semiconductor quantum dots take the role as the fluorophore. However organic dyes and quantum dots was limited by toxicity and photobleaching

Table 1
Aptasensors for detection of the $VEGF_{165}$.

Aptasensing Detection Strategy	Linear range (LR)	(LOD)	Ref.
Catalysis of Porphyrin controlling by aptamer	0–25 nM	1 ng mL^{-1}	(Li et al., 2015a)
Signal amplification by enzyme/(PQQ-GDH)/	1560 nM	15 nM	(Nonaka et al., 2012)
Antibody-aptamer sandwich assay	5 pg mL^{-1} to 1 ng mL^{-1}	401 pg mL^{-1}at 65 MHz	(Qureshi et al., 2015)
Fluorescence aptasensor based on graphene oxide	5–200 pM	1 p.M.	(Li et al., 2015b)
Quinone reporter/Fluorogenic hydrocyanine	100 fM and 10 pM	3.5 pg mL^{-1}	(Chattaraj et al., 2016)
TISS/MB aptamer	50 p.M. to 0.15 nM	5 p.M.	(Zhao et al., 2011)
Polarized Fluorescence detection recognition reaction	0.32–5.0 nM	2.48 nM	(Wang et al., 2014)
Imprinted polymer on electrode	0.01–7000 pg mL^{-1}	0.005 pg mL^{-1}	(Johari-Ahar et al., 2018)
Electroactive label (hemin)	0–80 nM	1 nM	(Lv et al., 2014)
	0–10 μM	6.2 nM	(Feng et al., 2016)
Graphene oxide-based FRET	5×10^{-10}–5×10^{-9} M	2.56×10^{-10}M	(Wang and Si, 2013)
Hemin DNAzyme/T7 exonuclease	1 pM to 20 nM	0.32 nM	(Zhang et al., 2015)
Isothermal amplification and DNA assembly switching	5–400 pg mL^{-1}	25 nM	(Li et al., 2017)
Aptamers Self-assembly of on gold-covered surface	0.15–100 ng mL^{-1}	0.15 ng mL^{-1}	(Crulhas et al., 2017)
(UCNPs) luminescence assay	50–2000 p.M.	6 pM	(Lan et al., 2016)
Sandwich assay based on dual aptamer	1–20 pg mL^{-1}	0.2 pM	(Shan et al., 2017)

characteristics. Metallic nanoclusters have been developed as a new class of fluorophore which illustrated color tenability, high surface to volume ratios and improved photophysical properties. Metal NCs have preferred alternatives over conventional organic fluorophores or quantum dots, due to large stokes shifts, lower toxicity, desirable biocompatibility, high photostability and ultrafine size. Among the noble nanoclusters, CuNCs have attracted a great deal of interest due to their specific photophysical properties, low cost and the higher earth abundance.

The comparison between the performance (LOD and linearity) of several studies in combination of QD or metallic nanocluster with aptamer as the aptasensing strategy for VEGF165 detection mentioned in Table 1. The advantages of represented signal-on nanoaptasensor in this study over the other aptasensing approach are simple synthesis procedure, one biosensing element, transducer and biorecognition element is one aptamer, enhancing the affinity of aptamer by avidity, mix and measure mechanism and improving fluorescent emission intensity with AIE and SAIE effects.

3.1. Design and characterization of TISS based bivalent aptamer for detecting $VEGF_{165}$

The $VEGF_{165}$ is a crucial biomarker in several diseases such as Age-related macular degeneration (AMD), Rheumatoid arthritis, Proteinuria, Diabetic retinopathy (DR) and Angiogenic stage of cancer tumor. This protein contains two domains; the Heparin-binding domain (HBD) and the receptor-binding domain (RBD). Aptamer based nanobiosensor is one of the novel robust technology for detecting the $VEGF_{165}$. There are several strategies for improving the affinity of aptamer which avidity is one of the most effective (Hasegawa et al., 2008b). The high-affinity aptamer could bind to Heparin-binding domain (HBD) or receptor-binding domain (RBD) (Ikebukuro et al., 2007). By multimerization, the aptamer could bind to HBD and RBD domains and the Kd in picomolar level obtained (Fukaya et al., 2015; Hasegawa et al., 2008a).

There are different categories for improving the aptamer-based biosensing such as Sandwich-Like Mode, Target-Induced Dissociation/Displacement (TID) Mode and Target-Induced Structure Switching (TISS) mode (Han et al., 2010). In Target-Induced Structure Switching (TISS) mode the aptamer bind to target directly and lead to changes in a specific pattern in three-dimensional conformation which has linear correlation along with detectable characteristic. The direct interaction of aptamer and analyte, which leads to a measurable signal without any further biosensing elements, made the TISS superior to other aptasensing systems like Sandwich-Like Mode and (TID).

In this study, The bivalent aptamer structure consists of 4 parts; poly T sequences on the both 3′ and 5′ ends for Cu nanoclusters nucleation and two different sequences which have affinity to $VEGF_{165}$ RBD and HBD domains. This structure can take the role as biorecognition and transducer moiety simultaneously due to a combination of $VEGF_{165}$ binding sequences and copper nucleation zones.

3.2. Thermodynamic analysis and secondary conformation prediction

For predicting the binding area loop and the effect of nucleation parts on aptamer secondary structure conformation, thermodynamic parameters of folding were calculated by Mfold web server (Zuker, 2003). Ten models for predicting secondary conformation were obtained. The most probable structure showed as Fig. 1A and the other nine models mentioned in the Supplementary material as Fig S1-S9. Free energy, enthalpy, entropy and paΔG were calculated as ΔH = -219.30 kcal/mol, ΔS = -661.7 cal/(K mol), paΔG = -14.07 kcal/mol at 37 °C. The Standard errors were roughly ± 5%. The calculated thermodynamic parameters in detail listed in S3 Table. Fig. 1A showed the secondary structure prediction based on the lowest free energy. The relevant angle for helices defined by the stems which branch from the loop orthogonal to the tangent of the circle. The diagram showed the likely impact of poly T tails in changing the conformation. The all ten secondary structure prediction models based on thermodynamic calculation were proved that poly thymine parts do not affect the secondary structure conformation and biosensing performance of whole aptamer.

The circle graph showed the overlap of bases (Fig. 1B). The basepair arrayed clockwise fashion and the perpendicular arc presented by the possible binding. The intersection arcs demonstrated the helices like line which showed the well-defined angle. As shown in the circle graph which is used for calculating the angle and prediction the stem-loop structure, there is no arc between poly T regions and the rest of bases in the both 3′ and 5′ ends.

The energy dot-plot showed the all possible folding superposition (Fig. 1C). The different suboptimality level demonstrated by colors in each dot in Fig. 1C. The base pair probability between nucleotide mentioned in i row and j column. The dots demonstrated the possible folding based on p% of ΔGmfe.

The superposition of all possible folding based on specified energy increment demonstrates by dot plot showed in Fig. 1D and the level of suboptimality presented in color on the presented triangular plot. As demonstrated in the whole ten models for ssDNA secondary structure prediction and Thermodynamic parameters calculation, the Cu nanocluster nucleation zones, poly thymine sequences, do not involve in making secondary structure conformation.

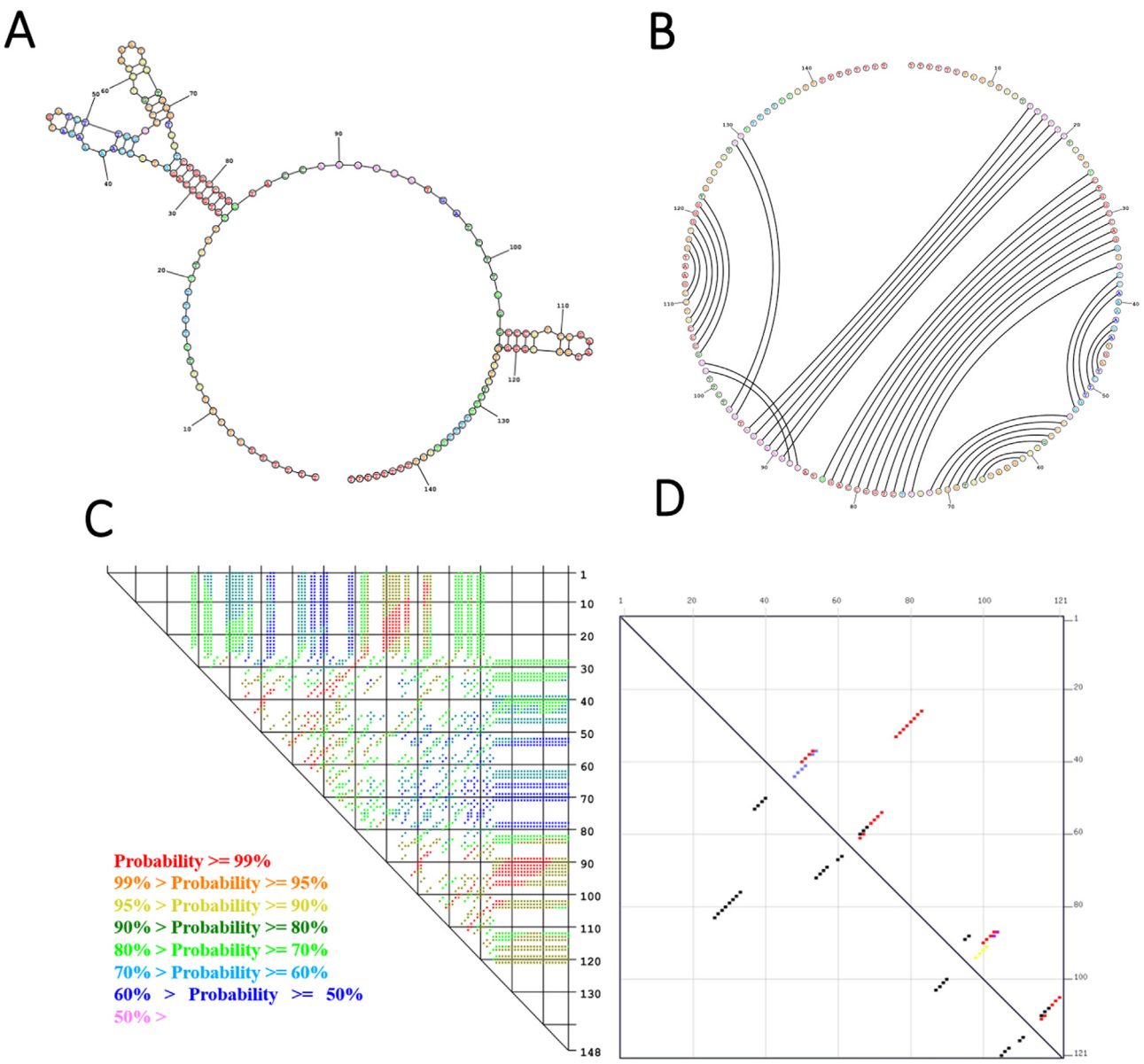

Fig. 1. Secondary structure based on probable basepairs predicted by thermodynamic parameters. A. The most probable secondary structure of bivalent aptamer based on lowest ΔH. **B.** circular diagram for secondary structure prediction **C.** Base pair binding probability diagram. **D.** the selected most probable binding of nucleotide. The different suboptimality level presented by colors in each dot demonstrated the base pair binding probability between nucleotide mentioned in i row and j column.

3.3. Characterization of the ssDNA hosted CuNC and aggregation dynamics studies

Controlling the supraparticle nanocluster formation and predefined area for accurate aggregation is challenging. By taking advantage of polyT sequence as template, accurate aggregation of the copper nanocluster became faesible. This study is first attempt to synthesize the stable Cu-NC supraparticles on specific regions of ssDNA. The procedure performed in two steps; First, $CuSo_45H_2O$ was reduced by L-Ascorbic acid and then, the reduced copper ion was added to ssDNA aptamer. As a result, the supraparticles were formed on the both 3′ and 5′ tails. The size, dispensability, hydrodynamic diameter and morphology of the B-Apt-CuNC aggregation in the presence of the 200 pM of $VEGF_{165}$ as the B-Apt-CuNC-$VEGF_{165}$ sample, were investigated by DLS, HRTEM, MALDI-TOF, and Electrophoresis techniques.

The Copper nanocluster building blocks constructed supraparticle on poly T ends and in Comparison with the single entity of colloidal Cu nanocluster, exhibited unique size-dependent properties such as photoluminescence and chirality. Fig. 2A and B demonstrated the remarkable effect of ssDNA scaffold in copper nanoclusters formation.

The effect of poly T tails of ssDNA aptamer on copper nanocluster supraparticle morphology investigated by the product of the first step reduction of Cupric sulfate (R-Cu) by L-Ascorbic acid as control. The uncontrolled aggregation and size polydispersity in R-Cu clearly showed in Fig. 2B. As shown in Fig. 2A, the microscopic image revealed the uniform molecular assembly of B-Apt-CuNC-$VEGF_{165}$. Two steps reduction procedure facilitated approaching the Cu nanocluster supraparticle formation on the both 3′ and 5′ ends.

As shown in Fig. 2A The Cu nanoclusters are building blocks of supraparticle arrays on ssDNA scaffold with a spherical shape and well-separated copper nanocluster. The presence of $VEGF_{165}$cause changes in three-dimensional conformation of the aptamer, consequently because of TISS effect the distance of supraparticles positioned in both 3′ and 5′ ends decreased and AIE and SAIE appeared, which is in

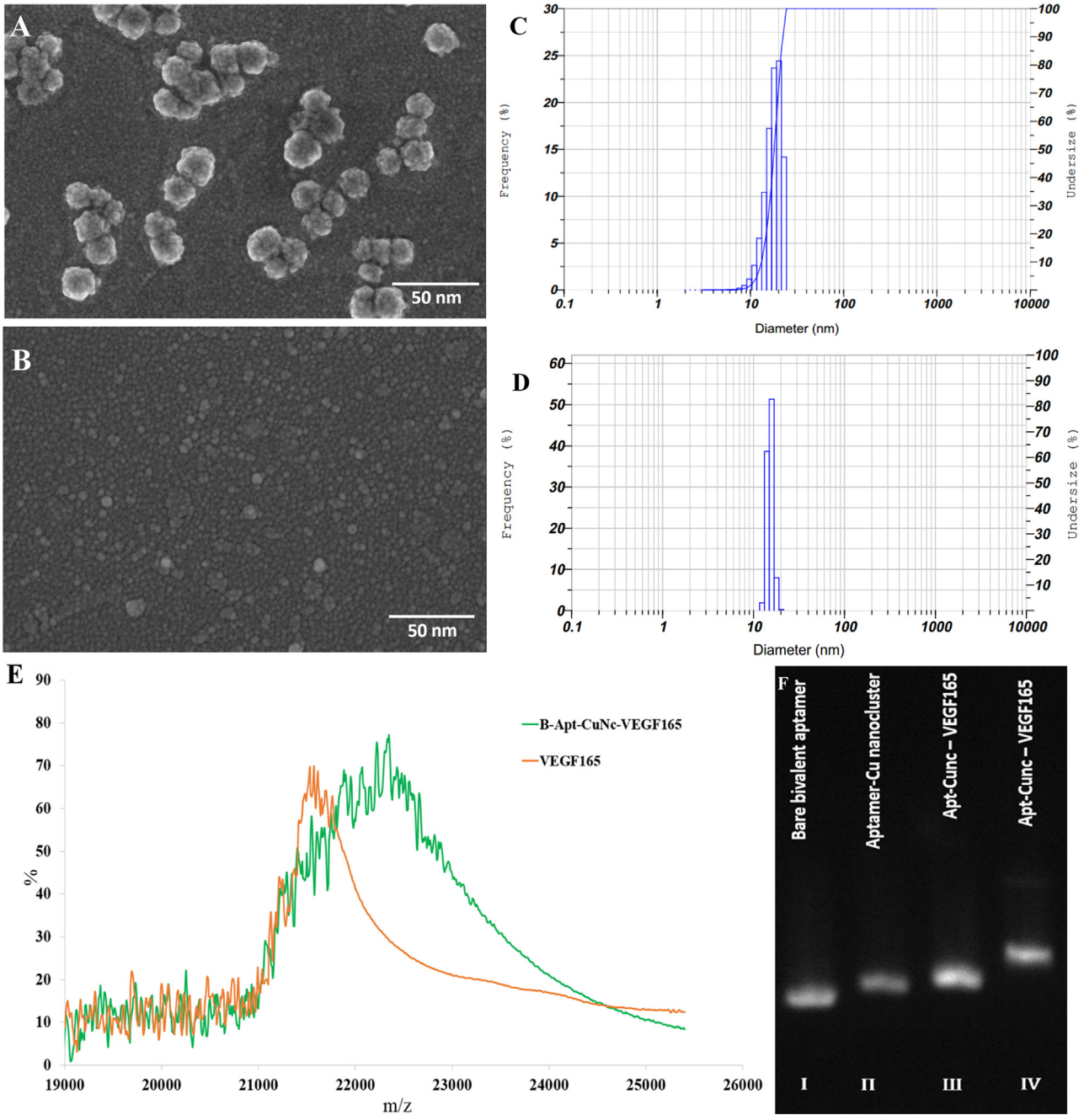

Fig. 2. The aggregation dynamics of the B-Apt-CuNC in the presence of the $VEGF_{165}$. A. Microscopic image of B-Apt-CuNC- $VEGF_{165}$ **B.** Microscopic image of the copper nanocluster in the absence of ssDNA aptamer. **C.** DLS results revealed the B-Apt-CuNC-$VEGF_{165}$ size distribution. **D.** DLS results showed the B-Apt-CuNC size distribution **E.** MALDI-TOF results showed the broadening peak of B-Apt-CuNC-$VEGF_{165}$ in comparison to $VEGF_{165}$ protein as a control. **F.** Characterization of the CuNC formed on ssDNA by electrophoresis. I) showed the bivalent bare ss-DNA aptamer as control, ii) the bivalent aptamer with copper nanocluster formed on both ends. iii and iv) the bivalent aptamer Cu-NC in the presence of $VEGF_{165}$ in 200 pM and 2000 pM as two different concentrations.

conformity with Dynamic Light Scattering (DLS) and spectroscopic studies results.

The size distributions of B-Apt-CuNC and B-Apt-CuNC-$VEGF_{165}$measured by dynamic light scattering (DLS). For investigating the effect of $VEGF_{165}$ presence on aggregation, the B-Apt-CuNC 1:15 dilution in HEPES buffer determined as control and the DLS spectra showed a very narrow size distribution and average size measured as 12.2 nm.

The size distribution of B-Apt-CuNC-$VEGF_{165}$ showed a range of 3.4 nm up to 19.8 nm. The average particle size of B-Apt-CuNC-$VEGF_{165}$ was calculated as 17.8 nm. The sharp peak of DLS in Fig. 2C indicated the monodispersity of aggregation and strong solubility of B-Apt-CuNC-$VEGF_{165}$, unlike the other AIE strategy which exhibited large aggregation with low stability and poor solubility in the aqueous suspension. The average hydrodynamic diameter of B-Apt-CuNC in the presence of 200 pM $VEGF_{165}$ was increased to 17 nm which is due to molecular assembly of B-Apt-CuNC-$VEGF_{165}$ with small hydrodynamic diameter centered at 5 nm.

The rising amount of nanocluster frequency in Fig. 2c indicated the compactness of B-Apt-CuNC-$VEGF_{165}$. Increasing in the frequency percentage showed the dominant numbers in aggregated structure and indicated a high sensitivity of B-Apt-CuNC to $VEGF_{165}$ (Fig. 2C).

MALDI-TOF was used for assessment the B-Apt-CuNC-$VEGF_{165}$ aggregation to clarify the effect of $VEGF_{165}$ presence. As shown in Fig. 2C,

free $VEGF_{165}$ 200 pM as the control sample demonstrated the distinctive peak at 21.2 kDa related to two 165AA polypeptide chains as disulfide-linked homodimeric protein. Through adding 200 pM $VEGF_{165}$ the ssDNA -protein complex formed, which leads to shift and broaden the spectrum peak as compared to pure $VEGF_{165}$ in 24 Kd.

As shown in Fig. 2E, the gel electrophoresis was performed for weight and charge assessment of the B-Apt-Cu-NC. The SAIE phenomena in the presence of $VEGF_{165}$ leads to heaviness and brightness in III and IV lanes in comparison with the lane No. II. Zhu and coworkers demonstrated which fluorescence copper nanocluster could stain DNA (Zhu et al., 2015). In this attempt, due to the formation fluorescence copper nanocluster on both 3′ and 5′ tails, the staining dyes (EtBr or gel Red) did not accomplish and the samples mixed with 15% of glycerol to induce heaviness in samples and loaded in lanes without further procedure. The bare aptamer was stained with Gel Red 6x as the control and loaded in the first lane. The movement direction of B-Apt-CuNC and B-Apt-CuNC-$VEGF_{165}$ to the positive pole through the 3% agarose gel showed negative charge of samples. Different positions related to third and fourth lanes revealed increasing in molecular weight of samples in 200 pM and 2000 pM concentration of $VEGF_{165}$.

3.4. the Target-induced structure switching (TISS) mode of the aptamer by CD investigation

Nanoclusters coupled on ssDNA induced optical characteristics. Electromagnetics energy transfer below the diffraction limit length occurs when the interparticle distance is less than the diameter in the close assembly of copper nanoclusters in a supraparticle structure in the presence of $VEGF_{165}$. The comparison in ellipticity of bare bivalent aptamer and the bivalent aptamer with copper nanoclusters showed a shift in peak as 6 nm at 270–276 nm in positive range and difference in 200–210 nm range (Fig. 3). The interaction between B-Apt-CuNC and $VEGF_{165}$ leads to loss in the inversion and mirror-symmetric and subsequently the chirality in negative Ellipticity in 208–224 nm obtained (Fig. 3). Lack of symmetry in aggregated B-Apt-CuNC-$VEGF_{165}$ induces the changes in secondary structure, dramatically. The B-Apt-Cu-NC-$VEGF_{165}$ optical active chiral molecule rotates the plane of plane-polarized light and demonstrates the broad peak in negative ellipticity.

3.5. The photophysical properties of B-Apt-CuNC-$VEGF_{165}$

The Cu-NC array has significant effect on energy transfer and photophysical performance. The random aggregation cause low fluorescent signal, instability and color impurity. By controlling the copper nanocluster aggregation, the luminescent enhancement has ensued. The homogeneous aggregation of the B-Apt-CuNC revealed a robust fluorescent signal. The interaction of B-Apt-CuNC with protein affects the excitation and emission dynamics. As shown in Fig. 4A and B, the B-Apt-CuNC showed excitation wavelength at 332 nm and the emission wavelength at 463 nm. Aggregation in the presence of $VEGF_{165}$ leads to restraining the intramolecular rotation and vibration of Cu-NC ligands. The radiative energy transfer rate increased due to suppression of the excited state nonradiative relaxation in B-Apt-CuNC- $VEGF_{165}$ and the excitation and emission wavelength changed to 390 nm and 524 nm. The coupling defined as the interaction of nanocluster with neighbors nearby showed the strong photophysical effect and large stock shift as 61 nm in this supraparticle nanostructure. This stock shift leads to reliable sensing signal with the minimum background signal.

As evidence in the absorbance wavelength which presented in Fig. 4b, there is no sign of sharp absorption peak in neither 260 nm nor 280 nm which are indicators for bare nucleic acid molecules. Several studies have reported a typical wavelength of 360 nm for Cu nanoclusters, but in this copper supraparticle DNA based structure, the max absorption wavelength was 333 nm. The spectra of B-Apt-CuNC in the presence of $VEGF_{165}$ showed a shift in absorption wavelength by 400 nm.

To investigate the effect of aptamer concentration and consequently B-Apt-CuNC concentration in fluorescence signal, three B-Apt-CuNC samples with different ssDNA concentrations (500 ng/μl, 1025.3 ng/μl, 1550.1 ng/μl) synthesized in HEPES buffer (300 μl, pH 7). As shown in Fig. 4C, the fluorescence intensity of B-Apt-CuNC in emission wavelength 463 nm, increased slightly with a linear relation between fluorescence intensity and ssDNA concentration. However, there is no shift in fluorescence signal observed by increasing the concentration.

Inter copper nanocluster distance is a critical parameter which has a high impact on metallophilic interaction (Hermann et al., 2001). Controlling the assembly aggregation and copper nanocluster compactness via a decrease in the average distance induces cuprophilic interaction and conduct to blue shift emitting which showed in Fig. 4D. By using the ssDNA as a template the distance is controlled accurately and SAIE effect induces enhancing the brightness and strong fluorescence signal. The solvatochromic effect due to change in solution condition related to the presence of $VEGF_{165}$ in post-synthesis stage, leads to blue emitting of CuNC which enhanced via the SAIE effect.

The quantum yield (QY) of the B-Apt-CuNC without the presence of $VEGF_{165}$ was calculated as 0.082 and in the presence of 200 pM of

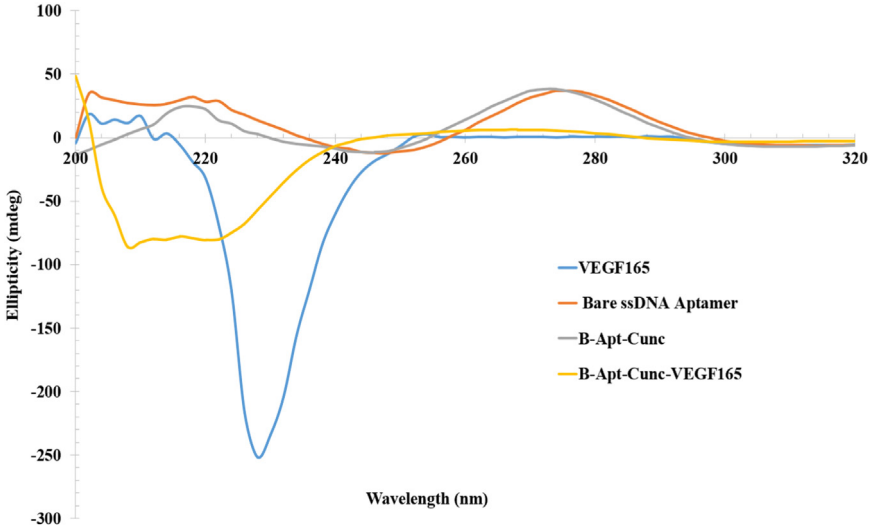

Fig. 3. Conformation study by Circular dichroism (CD). The CD spectra of the bare bivalent aptamer as control (red), B-apt-cu-NC (gray), $VEGF_{165}$ as control (blue), bivalent aptamer Cu nanocluster in the presence of $VEGF_{165}$ (yellow). The data normalized to HEPES buffer CD spectra.

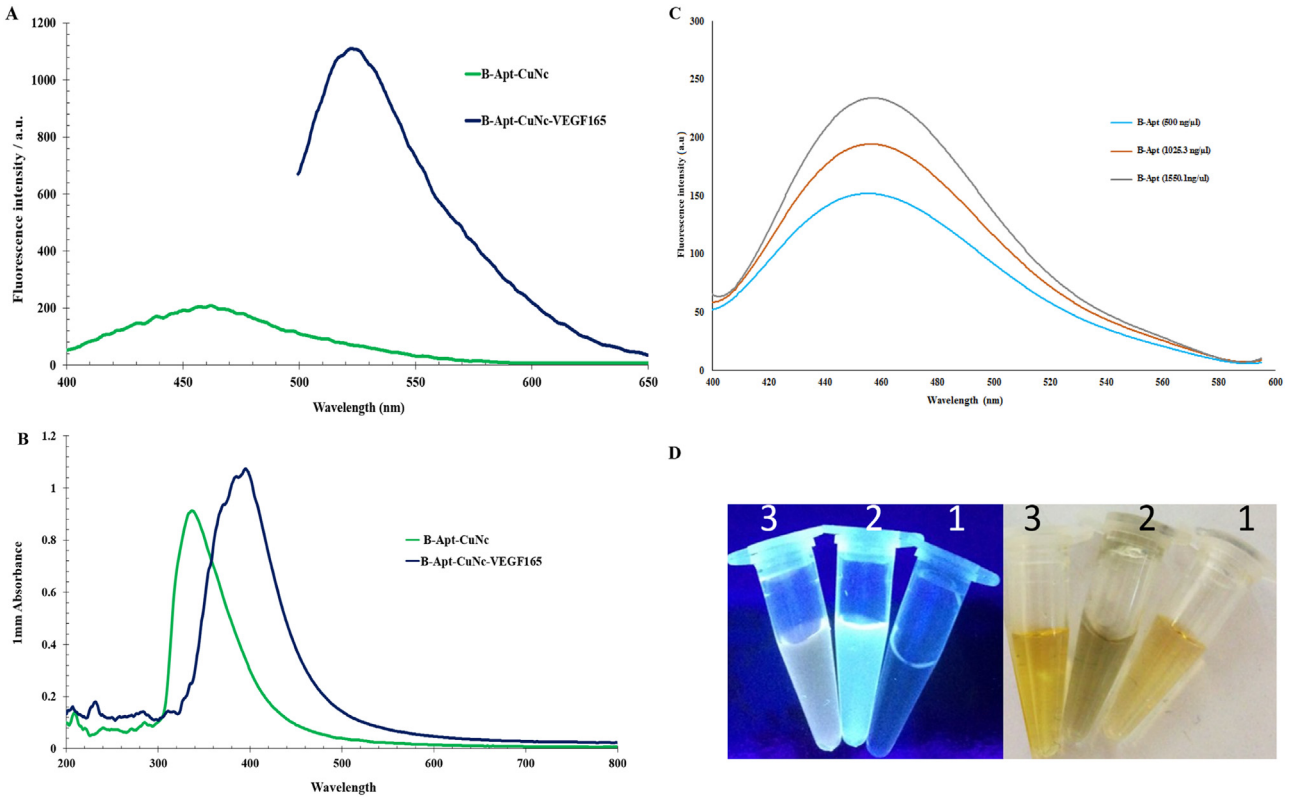

Fig. 4. A) Changes in the fluorescent emission wavelength for B-Apt-CuNC and B-Apt-CuNC-VEGF$_{165}$ were measured at 463 nm and 524 nm; B) Shift in UV–vis absorption spectra for B-Apt-CuNC and B-Apt-CuNC-VEGF$_{165}$ in 332 nm and 393 nm; C) the effect of B-Apt-CuNC concentration on fluorescence signal. D) Digital photographs in visible light (left) and under UV exposure (right), 1. Reduced Cu ions, 2. Apt Cu-NC with VEGF$_{165}$, 3. Apt Cu-NC without VEGF$_{165}$.

VEGF$_{165}$ reached a value of 0.124.

3.6. Analytical performance of the B-Apt-CuNC

The simple mechanism of this label-free nanobiosensor is designed based on "mix and measure" assay without complicated preparation procedure; the strong fluorescence signal appeared because of TISS, AIE and SAIE effects. The conformation changes of the bivalent aptamer as target recognition structure enhances the AIE effect and leads to the visible shift in color. The results of B-Apt-CuNC-VEGF$_{165}$ fluorescence studies on optimization the incubation Period (5–10 min −20–30 min −40–50 min −60 min) was shown in Fig. 5A the B-Apt-CuNC-VEGF$_{165}$ showed the fluorescence emission in 524 nm. By increasing incubation time from 5 to 40 min, The peak intensity increased. When the incubation time was equal to or greater than 40 min, the relative steady state was obtained. Based on the *t*-test results, the P-value between 5 min and 40 min was calculated as 0.01, revealed that emission intensity was significantly different. The P-value for 40–60 min was 0.30, illustrated no significant difference after 40 min incubation. Based on this result the incubation time of 40 min was applied to the all experiments.

The aptamer-based assay for testing the sensitivity was performed via fluorescence spectrometer by different concentration of VEGF$_{165}$ in range of 10–800 pM with 40 min incubation time. As revealed in Fig. 5B, the fluorescence intensity of B-Apt-CuNC-VEGF$_{165}$ continually increased in the higher concentration of VEGF$_{165}$ up to 800 pM. This manner represented the linear correlation (R^2 = 0.9943) between fluorescence intensity and VEGF$_{165}$ concentration which depicted in Fig. 5C. The regression equation was calculated with the VEGF$_{165}$ concentration (x) and fluorescence intensity (y). The LOD of this novel nanobiosensor was calculated by LOD = 3σ/k, where σ is the standard deviation and the slope of the calibration curve (k). The calculated LOD is 12 pM which revealed high sensitivity and the proportionate performance.

Eight different proteins were examined for selectivity assay by measuring the fluorescence intensity of B-Apt-CuNC in the presence of 200 pM of each non-target proteins including Human Serum Albumin protein (HSA), Bovine Serum Albumin Protein (BSA), The IGF-1, Recombinant Human HB, EGF protein, IgG and IgE. As shown in Fig. 5D, due to the high affinity of the bivalent aptamer to VEGF$_{165}$, enhancement in fluorescence intensity mainly occurred in the presence of this specific protein.

3.7. Detection the VEGF$_{165}$ in a human serum sample

The performance of this nanobiosensor evaluated by sensing the VEGF$_{165}$ in two serum samples (500 µl) from a healthy person and colorectal cancer patient. The experiments run in triplicate and data was reported on average. The B-Apt-CuNC (200 µl) incubated with Serum sample (500 µl) for 40 min in room temperature. The results for the colorectal cancer patient and the healthy one measured by proposed nanobiosensor as 680 pM and 150 pM of VEGF$_{165}$. For validating the functionality of the represented nanobiosensor, the control experiments run by a commercial kit which obtained serum VEGF$_{165}$ concentration of 683 pM for the colorectal cancer patient and 156 pM for the healthy person which demonstrated the reliability of the represented nanobiosensor.

4. Conclusions

In summary, a novel ultrasensitive signal-on nanobiosensor for detecting VEGF$_{165}$ was developed. The turn-on nanobiosensor was designed based on SAIE, AIE via TISS mode of bivalent aptamer. By adding the poly T sequence on both 3′ and 5′ to the bivalent aptamer as

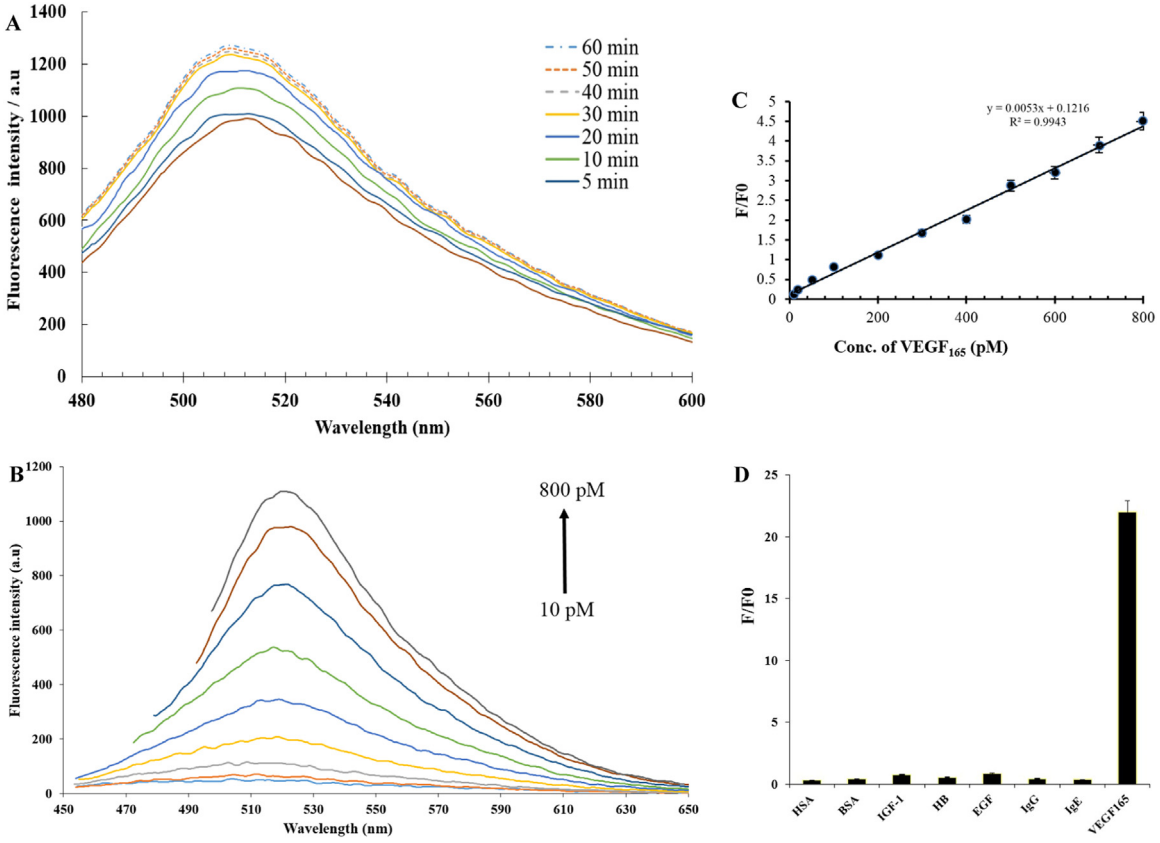

Fig. 5. A) Incubation time assessment (5–60 min). B) Enhancement in fluorescence intensity with $VEGF_{165}$ concentration(0.1–800 pM); C) The linear relationship between fluorescence intensity and $VEGF_{165}$ concentration; D) the selectivity assay of the presented nanobiosensor for $VEGF_{165}$.

the Cu nanocluster supraparticle formation area, the transducer and biorecognition element defined in one aptamer. The LOD and the linearity proportional to the $VEGF_{165}$ concentration were calculated as 12 pM and 10–800 pM The results related to real samples assessment depicted the accuracy and repeatability in comparison to results obtained from commercial kit. Our suggested method can open a new validated approach for quantification of protein biomarker through photometry assays.

CRediT authorship contribution statement

Fatemeh Mortazavi Moghadam: Conceptualization, Methodology, Validation, Investigation, Resources, Writing - original draft, Visualization. **Mahdi Rahaie:** Conceptualization, Methodology, Validation, Resources, Writing - original draft, Writing - review & editing, Visualization, Supervision, Project administration, Funding acquisition.

Acknowledgments

The authors acknowledge support from the University of Tehran and Iran Nanotechnology Initiative Council (INIC).

Declaration of interest statement

None.

Appendix A. Supplementary material

Supplementary data associated with this article can be found in the online version at doi:10.1016/j.bios.2019.02.046.

References

Alam, R., Mistri, T., Mondal, P., Das, D., Mandal, S.K., Khuda-Bukhsh, A.R., Ali, M., 2014. Dalton Trans. 43 (6), 2566–2576.
Bagheri, H., Afkhami, A., Khoshsafar, H., Hajian, A., Shahriyari, A., 2017. Biosens. Bioelectron. 89, 829–836.
Bus, P., Scharpfenecker, M., Van Der Wilk, P., Wolterbeek, R., Bruijn, J.A., Baelde, H.J., 2017. Diabetologia 60 (9), 1813–1821.
Chattaraj, R., Mohan, P., Livingston, C.M., Besmer, J.D., Kumar, K., Goodwin, A.P., 2016. ACS Appl. Mater. Interfaces 8 (1), 802–808.
Chen, C.K., Yu, W.H., Cheng, T.Y., Chen, M.W., Su, C.Y., Yang, Y.C., Kuo, T.C., Lin, M.T., Huang, Y.C., Hsiao, M., Hua, K.T., Hung, M.C., Kuo, M.L., 2016. Sci. Rep. 6, 31398.
Crulhas, B.P., Karpik, A.E., Delella, F.K., Castro, G.R., Pedrosa, V.A., 2017. Anal. Bioanal. Chem. 409 (29), 6771–6780.
Dehghani, S., Nosrati, R., Yousefi, M., Nezami, A., Soltani, F., Taghdisi, S.M., Abnous, K., Alibolandi, M., Ramezani, M., 2018. Biosens. Bioelectron. 110, 23–37.
Dutta, A., Goswami, U., Chattopadhyay, A., 2018. ACS Appl. Mater. Interfaces 10 (23), 19459–19472.
Feng, L.Y., Lyu, Z.Z., Offenhäusser, A., Mayer, D., 2016. Eng. Life Sci. 1–10.
Fukaya, T., Abe, K., Savory, N., Tsukakoshi, K., Yoshida, W., Ferri, S., Sode, K., Ikebukuro, K., 2015. J. Biotechnol. 212, 99–105.
Gast, R.E., König, S., Rose, K., Ferenz, K.B., Krieglstein, J., 2011. BMC Biochem. 12 (1), 28.
Han, K., Liang, Z., Zhou, N., 2010. Design strategies for aptamer-based biosensors. Sensors 10 (5), 4541–4557.
Hasegawa, H., Sode, K., Ikebukuro, K., 2008a. Biotechnol. Lett. 30 (5), 829–834.
Hasegawa, H., Taira, K.-I., Sode, K., Ikebukuro, K., 2008b. Sensors 8 (2), 1090–1098.
Hermann, H.L., Boche, G., Schwerdtfeger, P., 2001. Chem. – Eur. J. 7 (24), 5333–5342.
Ikebukuro, K., Hasegawa, H., Sode, K., 2007. Nucleic Acids Symp. Ser. 51, 399–400.
Johari-Ahar, M., Karami, P., Ghanei, M., Afkhami, A., Bagheri, H., 2018. Biosens. Bioelectron. 107, 26–33.
Ju, M., Mailhos, C., Bradley, J., Dowie, T., Ganley, M., Cook, G., Calias, P., Lange, N., Adamis, A.P., Shima, D.T., Robinson, G.S., 2008. Investig. Ophthalmol. Vis. Sci. 49 (2), 662–670.
Kong, R.-M., Ding, L., Wang, Z., You, J., Qu, F., 2015. Anal. Bioanal. Chem. 407 (2), 369–377.
Lan, J., Li, L., Liu, Y., Yan, L., Li, C., Chen, J., Chen, X., 2016. Microchim. Acta 183 (12), 3201–3208.
Li, J., Sun, K., Chen, Z., Shi, J., Zhou, D., Xie, G., 2017. Biosens. Bioelectron. 89, 964–969.
Li, W., Zhang, Q., Zhou, H., Chen, J., Li, Y., Zhang, C., Yu, C., 2015a. Anal. Chem. 87 (16), 8336–8341.

Li, X., Ding, X., Fan, J., 2015b. Analyst 140 (23), 7918–7925.
Liu, Y., Yao, D., Zhang, H., 2018. ACS Appl. Mater. Interfaces 10 (15), 12071–12080.
Lv, Z., Wang, K., Zhang, X., 2014. J. Immunoass. Immunochem. 35 (3), 233–240.
Mahmoudi, E., Hajian, A., Rezaei, M., Afkhami, A., Amine, A., Bagheri, H., 2019. Microchem. J. 145, 242–251.
Makarevich, P.I., Boldyreva, M.A., Gluhanyuk, E.V., Efimenko, A.Y., Dergilev, K.V., Shevchenko, E.K., Sharonov, G.V., Gallinger, J.O., Rodina, P.A., Sarkisyan, S.S., Hu, Y.C., Parfyonova, Y.V., 2015. Stem Cell Res. Ther. 6, 204.
Nonaka, Y., Abe, K., Ikebukuro, K., 2012. Electrochemistry 80 (5), 363–366.
Qu, F., Pei, H., Kong, R., Zhu, S., Xia, L., 2017. Talanta 165, 136–142.
Qureshi, A., Gurbuz, Y., Niazi, J.H., 2015. Sens. Actuators B: Chem. 209, 645–651.
Shan, S., He, Z., Mao, S., Jie, M., Yi, L., Lin, J.-M., 2017. Talanta 171, 197–203.
Stoll, H., Steinle, H., Wilhelm, N., Hann, L., Kunnakattu, S.-J., Narita, M., Schlensak, C., Wendel, H.P., Avci-Adali, M., 2017. Molecules 22 (6), 954.
Wang, R., Crystal, R.G., Hackett, N.R., 2009. BMC Mol. Biol. 10 (1), 103.
Wang, S.E., Huang, Y., Hu, K., Tian, J., Zhao, S., 2014. Anal. Methods 6 (1), 62–66.
Wang, S.E., Si, S., 2013. Appl. Spectrosc. 67 (11), 1270–1274.
Wintzheimer, S., Granath, T., Oppmann, M., Kister, T., Thai, T., Kraus, T., Vogel, N., Mandel, K., 2018. ACS Nano.
Yang, H.-W., Ju, S.-P., Cheng, C.-H., Chen, Y.-T., Lin, Y.-S., Pang, S.-T., 2018. Biosens. Bioelectron. 119, 25–33.
Zhang, H., Li, M., Li, C., Guo, Z., Dong, H., Wu, P., Cai, C., 2015. Biosens. Bioelectron. 74, 98–103.
Zhang, X., Kong, R., Tan, Q., Qu, F., Qu, F., 2017. Talanta 169, 1–7.
Zhao, S., Yang, W., Lai, R.Y., 2011. Biosens. Bioelectron. 26 (5), 2442–2447.
Zhu, X., Shi, H., Shen, Y., Zhang, B., Zhao, J., Li, G., 2015. Nano Res. 8 (8), 2714–2720.
Zuker, M., 2003. Nucleic Acids Res. 31 (13), 3406–3415.